

Field off Scattering Studies in Lithium Hydride

Ryan Bayes
The MICE collaboration

Multiple coulomb scattering is a well known electromagnetic phenomenon experienced by charged particles traversing materials. However, from recent measurements by the MuScat experiment it is known that the available simulation codes, specifically GEANT4, overestimate the scattering of muons in low Z materials. This is of particular interest to the Muon Ionization Cooling Experiment (MICE) which has the goal of measuring the reduction of a muon beam emittance induced by energy loss in low Z absorbers. Multiple scattering induces positive changes in the emittance in contrast to the reduction due to ionization energy loss. It therefore is essential that MICE measures multiple scattering for its absorber materials; lithium hydride and liquid hydrogen; and validate the multiple scattering against known simulations. MICE took data with magnetic fields off suitable for multiple scattering measurements in the fall of 2015 using a Xenon filled LH2 cask and spring of 2016 using the lithium hydride absorber. The data was compared to a convolution between data collected with no absorber and specific models of scattering in lithium hydride, including the default GEANT4 model. A deconvolution procedure was also applied to the data to extract the scattering distribution within the absorber material. The results for the comparisons and the deconvolved scattering widths are reported for the three nominal beam momenta; 172 MeV/c, 200 MeV/c, and 240 MeV/c. A momentum dependent measurement of multiple scattering in lithium hydride was also conducted and the result was compared to muon beams used to collect the lithium hydride data allow momentum dependent measurements of the scattering to be conducted and compared with the accepted scattering model.

1 Introduction

MICE intends to make a measurement of emittance reduction in low Z absorbers such as liquid hydrogen and lithium hydride. The beam emittance is increased by the scattering in the absorber material. The change in the emittance [1] is given by

$$\frac{d\epsilon_n}{dz} \approx -\frac{\epsilon_n}{p_\mu\beta} \left\langle \frac{dE_\mu}{dz} \right\rangle + \frac{\beta_\perp p_\mu}{2m} \frac{d\Theta^2}{dz} \quad (1)$$

where Θ is the RMS scattering width, $\frac{dE}{dz}$ is the energy loss of a muon, ϵ_n is the normalized emittance $\epsilon_n = \sqrt{\det(\text{Var}(x, y, p_x, p_y))}/m_\mu$, m_μ is the muon mass, p_μ is the muon momentum, $\beta = v_\mu/c$ is the relativistic velocity of the muon, and β_\perp is the extent of the transverse momentum distribution. Multiple scattering is not well modelled for low Z absorbers in the standard simulations. Data collected by the MuScatt experiment [2] indicates that GEANT overestimates the scattering for these materials[3]. For MICE to make believable predictions of the emittance in the absorber materials a the model in the simulation must be validated, or a new model must be introduced that provides a better reflection of what exists in data. This is particularly important for the prediction of the equilibrium emittance; the case where there is no change in emittance or when

$$\epsilon_n = \frac{\beta_\perp p_\mu^2}{2m} \frac{d\Theta^2}{dz} \left\langle \frac{dE_\mu}{dz} \right\rangle^{-1}. \quad (2)$$

This provides the minimum emittance for which cooling is effective.

1.1 Definitions

Multiple scattering is characterized using either the angle between the initial and final momentum vectors or the difference of angles that those vectors make when projected onto a given coordinate plane. The former is perhaps more intuitive and is expressed mathematically as

$$\theta_{Scatt} = \text{acos} \left(\frac{\mathbf{p}_{US} \cdot \mathbf{p}_{DS}}{|\mathbf{p}_{US}| |\mathbf{p}_{DS}|} \right) \quad (3)$$

where \mathbf{p}_{US} and \mathbf{p}_{DS} are the momentum vectors measured by the upstream and downstream trackers, respectively. Alternatively the projection of the scattering angle onto the X-Z or Y-Z plane may be considered. This can be defined by considering the inner product of the downstream momentum with the component of the upstream momentum vector perpendicular to the projection plane vector. For example the scattering projection into the plane defined by the momentum vector and the z-axis should be

$$\theta_y = \text{atan} \left(\frac{\mathbf{p}_{DS} \cdot (\hat{\mathbf{y}} \times \mathbf{p}_{US})}{|\hat{\mathbf{y}} \times \mathbf{p}_{US}| |\mathbf{p}_{DS}|} \right) \quad (4)$$

where $\hat{\mathbf{y}}$ is the unit vector in the y direction. A scattering angle in the perpendicular plane must then be defined as

$$\theta_x = \text{atan} \left(\frac{\mathbf{p}_{DS} \cdot (\mathbf{p}_{US} \times (\hat{\mathbf{y}} \times \mathbf{p}_{US}))}{|\mathbf{p}_{US} \times (\hat{\mathbf{y}} \times \mathbf{p}_{US})| |\mathbf{p}_{DS}|} \right) \quad (5)$$

where $\hat{\mathbf{y}}$ is the unit vector in the x direction. These two expressions can be expressed in terms of the gradients of the muon tracks before and after the scatters;

$$\theta_y = \text{atan} \left(\frac{\sqrt{1 + \frac{dx^2}{dz_{US}^2} + \frac{dy^2}{dz_{US}^2}}}{\sqrt{1 + \frac{dx^2}{dz_{US}^2}}} \left\{ \frac{\frac{dx}{dz}_{DS} - \frac{dx}{dz}_{US}}{1 + \frac{dx}{dz}_{US} \frac{dx}{dz}_{DS} + \frac{dy}{dz}_{US} \frac{dy}{dz}_{DS}} \right\} \right) \quad (6)$$

$$\theta_x = \text{atan} \left(\sqrt{\frac{1 + \frac{dx^2}{dz_{US}^2} + \frac{dy^2}{dz_{US}^2}}{(1 + \frac{dx^2}{dz_{US}^2} + \frac{dy^2}{dz_{US}^2})(1 + \frac{dx^2}{dz_{US}^2})}} \left\{ \frac{\frac{dy}{dz}_{DS}(1 + \frac{dx^2}{dz_{US}^2}) - (\frac{dx}{dz}_{DS} \frac{dx}{dz_{US}} - 1) \frac{dy}{dz_{US}}}{1 + \frac{dx}{dz_{US}} \frac{dx}{dz}_{DS} + \frac{dy}{dz_{US}} \frac{dy}{dz}_{DS}} \right\} \right) \quad (7)$$

In the approximation of small angles (i.e. $\frac{dx}{dz} \approx \frac{dy}{dz} \ll 1$) these produce the more familiar forms;

$$\theta_x = \frac{dy}{dz_{US}} - \frac{dy}{dz_{DS}} \quad (8)$$

for scattering about the x-axis or

$$\theta_y = \frac{dx}{dz_{US}} - \frac{dx}{dz_{DS}} \quad (9)$$

for scattering about the y-axis. The more exact expressions will be used for this analysis.

1.2 Scattering Predictions for MICE

The behaviour of the coulomb scattering is a material dependent quantity which has been described by the radiation length X_0 . Greisen and Rossi derived an expression for the RMS scattering width that has been further developed by other authors and is expressed in by the particle data group as

$$\Theta = \frac{13.6 \text{ MeV/c}}{p_\mu \beta} \sqrt{\frac{z}{X_0}} \left(1 + 0.038 \ln \frac{z}{X_0} \right). \quad (10)$$

where z is the material thickness, and X_0 is expressed in cm. The $\left(1 + 0.038 \ln \frac{z}{X_0}\right)$ term is an empirical correction for the material dependence of the expression. Equation 1 is applicable to the projections of the multiple scattering angles on the X-Z or Y-Z plane. Thus it should be related to the scattering angle in space by a factor of $\sqrt{2}$, or $\Theta_X^2 + \Theta_Y^2 \approx \Theta_{Scatt}^2$. Multiple scattering produces a distribution that is Gaussian with respect to the projected scattering angles for small angles. For small angles Eq.10 is valid at the 1% for most materials.

The MICE LiH absorber is a disk, 65 mm in length (along the Z axis) with a 55 cm diameter with a composition of 81% ^6Li , 4% ^7Li , 14% ^1H with some trace amounts of Carbon, Oxygen and Calcium. The density of this disk has been measured to be $0.694 \pm 0.003 \text{ g/cm}^3$ based on measurements of a test mass with uncertainties of 1 g and the dimensions of 0.254 mm. Simulations using the correct composition contrasted with the use of an absorber composed of ^7Li (with a density of 0.79 g/cm^3) shows no difference in scattering, so the precise isotopic composition of the absorber is not significant to the measurements described here. With this in mind, the scattering distribution widths predicted by Eq.10 for the absorber material and the other materials in the channel are shown in Table 1. This shows that the vast majority of the scattering in the MICE channel takes place in the absorber.

Comparisons with Eq. 10 are not sufficient; the purpose of these measurements is to compare the scattering to that in simulation and to evaluate the distributions for all accessible angles. Geant 4[4] as part of its default physics list, uses the "Wentzel VI" model for multiple scattering at all angles for muons, pions, kaons, protons, and anti-protons at all energies. This model uses the scattering probability differential in the solid angle ω and the material thickness z .

$$\Xi(\theta)d\omega dz = 4N_a \frac{Z^2}{A} r_e^2 \left(\frac{m_e c}{\beta p}\right)^2 \frac{d\omega}{(\theta_1^2 + \theta^2)^2} dz \quad (11)$$

for a number of atoms N_a with atomic number Z and atomic weight A given an incident particle with momentum p and $\beta = p/E$ which can then be integrated over solid angle ω to produce a rate of change of the mean square scattering angle

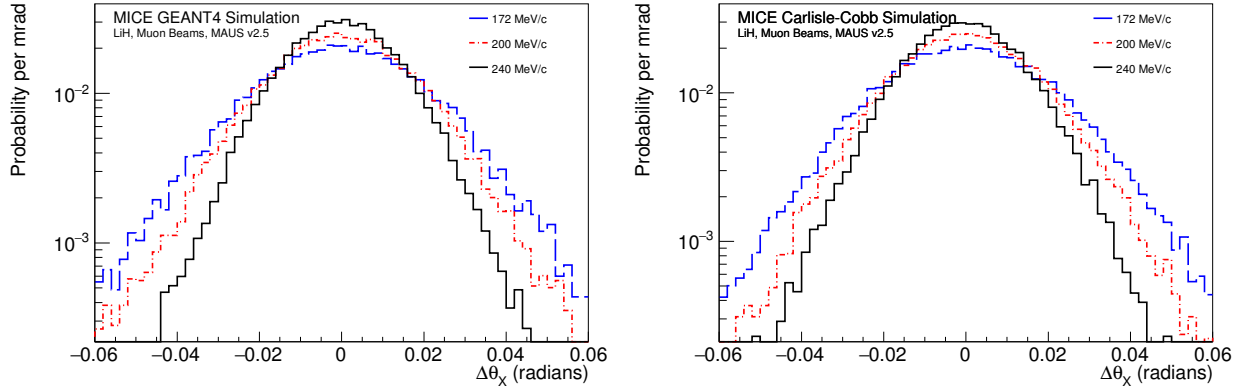
$$\frac{d\theta^2}{dz} = 4N_a \frac{Z^2}{A} r_e^2 \left(\frac{m_e c}{\beta p}\right)^2 \left(\ln \left[\left(\frac{\theta_2}{\theta_1}\right) + 1 \right] - 1 + \frac{1}{Z} \left(\ln \left[\left(\frac{\theta_2}{\theta_1}\right)^2 + 1 \right] - 1 \right) \right). \quad (12)$$

assuming that the scattering cross-section for nuclei and electrons is the same. In the above equations θ_1 and θ_2 are the integration minimum and maximum angles. GEANT uses a compact implementation[5] of the model to simulate the distribution; that is it uses a representation of the scattering distributions to replicate the scattering behaviour of particles over a given step through a material rather than simulating single interactions. The scattering distributions of muons in lithium hydride at three different momenta as predicted by GEANT are shown in Fig. 1a. For comparison the scattering at 240 MeV/c in Xenon gas at standard temperature and pressure is shown in Fig. ??.

An alternative implementation was worked out as part of Tim Carlisle's thesis[6], known therein as the XYZ model, but it shall be referred to here as the Carlisle-Cobb (CC) model. This is an implementation of the Wentzel model that uses a brute force, atomistic approach to generate the scattering distributions—each separate interaction within a material is sampled. The predicted scattering distributions of muons in lithium hydride at three different momenta using the CC implementation are shown in Fig. 1b. Again the implementation for Xenon gas is shown in Fig.?. In difference to LiH, there is a stark contrast in the Xenon absorber between the Carlisle-Cobb simulation and the GEANT4 simulation. The cause for the difference is not known.

Table 1: Material budget affecting tracks passing through the MICE LiH absorber. The material thickness normalized by the radiation length is given with the RMS of the scattering distribution calculated from the full PDG formula. Note that the effective thickness shown for the tracker materials (He and Scint. Fibres) is for one tracker.

Material	z(mm)	z/X_0	Θ (mrad)		
			172 MeV/c	200 MeV/c	240 MeV/c
LiH	65	0.064	25.9	21.5	17.3
Tracker He	113	0.00015	1.5	1.3	1.0
Al Window	0.016	0.00179	4.9	4.0	3.3
Scint. Fibres	0.74	0.0175	14.2	11.7	9.5
Total			30.0	24.8	20.0



(a) Scattering distributions generated by GEANT4 in (b) Scattering distributions generated using the Cobb lithium hydride. Carlisle implementation in lithium hydride.

Figure 1: Scattering distributions generated using different multiple scattering implementations.

Table 2: Data collected for the purpose of measuring muon scattering in MICE in December of 2015 and February, March of 2016 listed by beam line setting.

(a) Data runs collected for field off multiple scattering

Zero Absorber			LiH Absorber					
3-172 MeV/c	3-200 MeV/c	3-240 MeV/c	3-172 MeV/c		3-200 MeV/c		3-240 MeV/c	
7666	7469	7516	7764	7826	7726	7807	7727	7817
7675	7652	7517	7766	7827	7729	7834	7733	7818
7676	7672	7674	7767	7831	7735	7835	7737	7819
7680	7673	7682	7694	7832	7736	7836	7738	7844
7683	7681	7685	7782	7861	7754	7838	7775	7847
7684	7695	7691	7783	7863	7770	7841	7776	7848
7690	7696	7693	7785	7864	7771	7842	7790	7849
7692		7768	7786	7865	7772	7843	7794	7851
			7787	7866	7773		7795	7852
			7799		7778		7796	7853
			7800		7784		7805	7854
			7806		7788		7808	7855
			7822		7789		7809	7856
			7823		7797		7813	7858
			7824		7798		7814	7859
			7825		7804		7816	7860

(b) Data and simulation triggers collected for the analysis.

State	Data		Simulation	
	TOF1	TOF2	TOF1	TOF2
Zero Abs. 172 MeV/c, Muon	624577	94722	771720	127245
Zero Abs. 200 MeV/c, Muon	384909	56314	370079	51822
Zero Abs. 240 MeV/c, Muon	314739	62546	1204155	261244
LiH 172 MeV/c, Muon	1282488	174405	718185	108777
LiH 200 MeV/c, Muon	1223560	177460	364587	45638
LiH 240 MeV/c, Muon	1239827	232982	1266073	236582

Table 3: Simple particle selection criteria for data with survival rates for 240 MeV/c data and simulation in LiH.

Selection	Description	μ Beams, LiH abs.			π Beam
		172	200	240	240
TOF1 trigger	At least two raw TOF slab hits exist and at least one in each TOF plane.	1.	1.	1.	1.
Upstream track selection	There is one US track and at most one track in the DS tracker (If is are no DS track $\theta_X = \theta_Y = 45^\circ$).	66.8%	68.4%	74.1%	59.0%
TOF timing selection	Select muons from run at the target momentum.	3.8%	5.4%	7.5%	35.0%
Fiducial selection	For projected US tracks $\sqrt{x^2 + y^2} < r_0$ at DS ref plane, where $x = x_0 + (\frac{dx}{dz} + a_0 \cos \phi)\Delta z$, $y = y_0 + (\frac{dy}{dz} + a_0 \sin \phi)\Delta z$, and $\phi = \tan^{-1} \frac{dy/dz}{dx/dz}$. $r_0 = 150$ mm and $a_0 = 0.012$ assumed.	0.3%	0.5%	0.8%	2%

2 Data Collection

Six data sets were compiled during the ISIS user cycle 2015/04 at three different momenta; 172 MeV/c, 200 MeV/c, and 240 MeV/c; with and without the lithium hydride (LiH) absorber in place. These data sets were collected in a rotating manner so that systematic behaviours that may have appeared in ISIS running could be balanced over the three nominal momenta. Table 2b shows the number of events that produce space points in TOF1 and TOF2 for the collected runs.

Data reconstruction and simulation was completed using MAUS 2.6.1. There is a deviation between data and simulation such that there is an offset of the simulated beam by +4 cm which is the southward direction in the hall coordinate system with an accompanying skew in the angular distribution. It is difficult to compare the data to the simulation explicitly because a skew in the beam distribution will produce a skew in the scattering distribution. In addition exaggerated high angle tails have been observed in the simulation particles passing through gas which are not seen in the data. For these reasons the simulation was not heavily relied upon for this analysis. The bulk of the analysis relies on the data collected with the absorber to provide the scattering measurement and data without the absorber to provide an independent measurement of the detector reconstruction and beam behaviour. The simulation is then used for the prediction of scattering in the absorber material.

3 Particle Selection

Prior to any higher order analysis a set of particles that are most likely to provide an unbiased scattering distribution must be selected from the data sample. The set of cuts used for the analysis is provided in Table ?? with the proportion of events selected from the absorber data sets. Only events that produce a space point in TOF1 and a trajectory in the upstream tracker are considered.

3.1 Downstream Track Detection

A measurement of scattering requires a trajectory reconstructed in the downstream tracker. An event cannot be rejected outright however if the downstream trajectory is absent for two reasons; normalization of the scattering distribution and to allow the possibility of correcting of the acceptance. In the absence of a reconstructed track downstream of the absorber, an angle of $\pi/4$, well outside of the channel acceptance, is assigned to the event so that the scattering angle appears in an overflow bin. A reconstruction acceptance can be estimated from the simulation by taking the ratio between the number of events for a true angle between θ_i and $\theta_i + \Delta\theta$. The reconstruction acceptance as a function of the projected scattering angles θ_X and θ_Y are shown in Fig.2. The acceptance before and after the full event selection is shown to demonstrate that the selection does not introduce a bias in the selection. The acceptance appears to be a constant 70% with respect to angle for 200 MeV/c muons.

Figure 2

3.2 TOF Selection and Momentum

If the particle has a time of flight between stations 0 and 1 (Δt_{01}) that falls outside of a window the particle is rejected. Time of flight distributions for the three beam settings are shown in Fig. 3a. The time of flight is used to select muons from the beam with a given momentum at the absorber as there is a monotonic relationship between these variables assuming that the particle mass is known. The momentum in the channel is calculated for a trajectory from the time of flight between stations 1 and 2 (Δt_{12}) assuming that all particles are travelling axially such that

$$p_{rec} = \frac{m_\mu c}{\sqrt{\frac{c\Delta t_{12}}{d} - 1}} \quad (13)$$

where m_μ is the muon mass, c is the speed of light and d is the distance between TOF stations 1 and 2, which was 8.62 m at the time in question. Off axis tracks will have a longer time of flight so a correction factor equal to $1/\sqrt{1 + (dx/dz)^2 + (dy/dz)^2}$ was applied to p_{rec} for each muon.

The momentum measured in this way is expected to have a bias due to either energy loss or instrumental effects. To determine the magnitude of the bias, a two dimensional histogram of the true momentum prior to entering the absorber versus the momentum reconstructed from Δt_{12} with a TOF cut applied to exclude electrons. The mean true momentum can then be fit using a straight line to provide a relationship between the reconstructed momentum of a muon and its momentum prior to scattering in the absorber. This procedure is illustrated for the sum of the simulations of the 172 MeV/c, 200 MeV/c, and 240 MeV/c data sets in Figure ??.

The relationship between the reconstructed and absorber momentum is slightly different for each of the three data sets as shown in Table ?. Δt_{01} as a function of the reconstructed momentum is shown in Fig. ?? prior to the calibration. Fig. ?? shows Δt_{01} as a function of the calibrated momentum where the calibration is applied separately for each data set based on the results of Table ?. A fit of $a/p_{cal} + b$ to Δt_{01} provides the TOF bins associated with the nominal momenta as defined in Table 3

3.3 Fiducial Selection of Events

Although a muon that produces an upstream track but not a downstream track is still counted

Finally, if the upstream track is projected to the downstream tracker station 1 and that track falls outside of the active radius of the detector, that particle is rejected. The active radius of the trackers is 150 mm. The predicted scattering for a 172 MeV/c beam is 24 mrad through the absorber. To select upstream tracks that are suspected to produce downstream tracks contained within the tracker volume, all tracks are projected from the upstream tracker to the downstream tracker with an additional radial component added to the projection vector consistent with half of the predicted scattering width or 12 mrad. If the radial position of the projected track at the downstream tracker is greater than 150 mm then the track is rejected.

Table 4: Time of flight selections between stations 0 and 1 made to correspond to specific axial momenta as measured by the time of flight between stations 1 and 2.

(a) TOF for Muon Beams				
Momentum (MeV/c)	lower limit (ns)	upper limit (ns)	Calculated $\langle p \rangle$ (MeV/c)	RMS (MeV/c)
172	29.154	29.354	172.11 ± 0.03	4.76 ± 0.02
200	28.286	28.486	199.95 ± 0.04	7.38 ± 0.03
240	27.465	27.665	239.95 ± 0.05	10.34 ± 0.03
(b) TOF for Pion Beam				
Momentum (MeV/c)	lower limit (ns)	upper limit (ns)	Calculated $\langle p \rangle$ (MeV/c)	RMS (MeV/c)
240	27.099	27.699	240.04 ± 0.09	11.45 ± 0.06

The effect of the selection criteria on the position and angle distributions in the 3-200 MeV/c data appear in Fig.5 and Fig.7 respectively. The scattering distributions for the LiH data appears in Fig.8a, for and for data taken with no absorber in Fig.8b.

4 Analysis

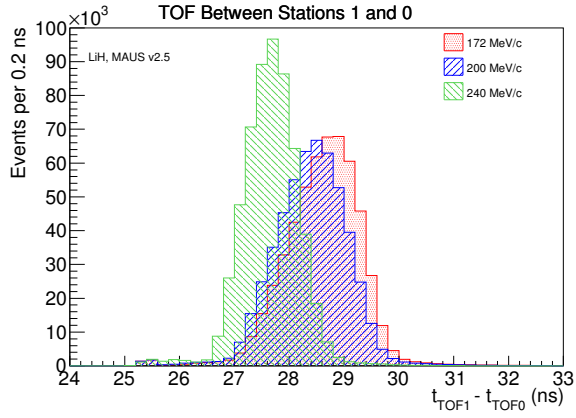
4.1 Convolution with Alternative Models

The simplest approach for comparing data to simulation is to convolve the data from the zero absorber runs with the scattering distributions from various models and compare the result with the data including the absorber. The convolution is achieved by adding an angle sampled from the predicted scattering distribution in the absorber, shown in Fig. 1, to the angles determined from a given trajectory selected from the zero absorber data. The trajectory described with the sum of angles is extrapolated to the downstream tracker and those trajectories that do not appear in the downstream tracker are then treated as overflow events.

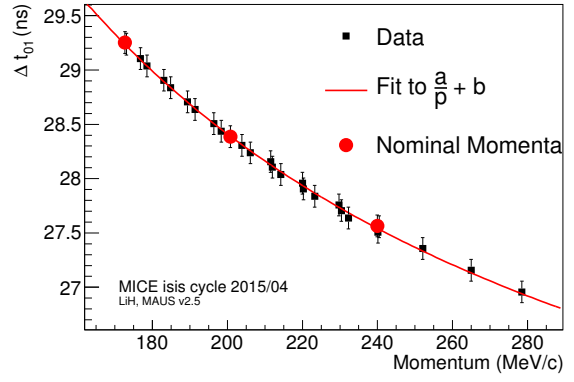
Because the zero absorber data sets are much smaller than the LiH data sets, the convolution was completed by sampling 10 different random angles from the source distribution for every data track selected from the empty absorber data. The resulting events are not statistically correlated so this procedure should have no impact on the treatment of statistical errors.

The analysis then consists of looking at the residuals between the two and determining which model is the best fit to the reconstructed data. This difference is expressed using

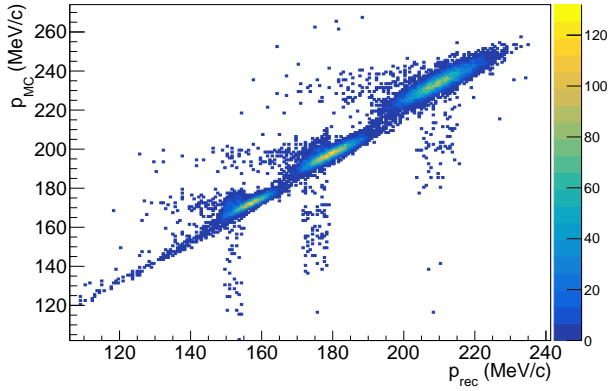
$$\chi^2 = \sum_{i=0}^N \frac{(n_{data}(\theta_i^{rec}) - n_{conv.}(\theta_i^{rec}))^2}{n_{data}(\theta_i^{rec}) + n_{conv.}(\theta_i^{rec}) + \sum \sigma_{sys,j}^2} \quad (14)$$



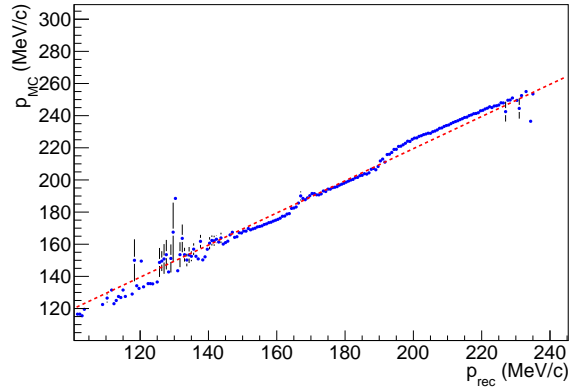
(a) TOF distributions of muon beams.



(b) Mean momentum by TOF

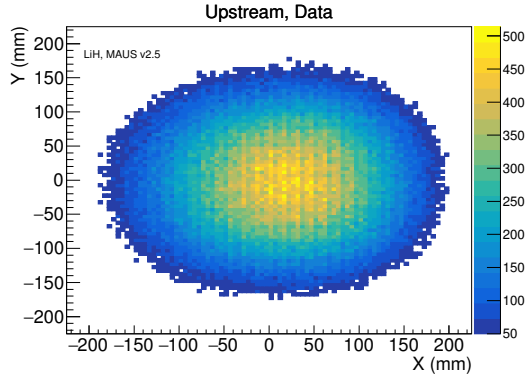


(c) Momentum response in simulation.

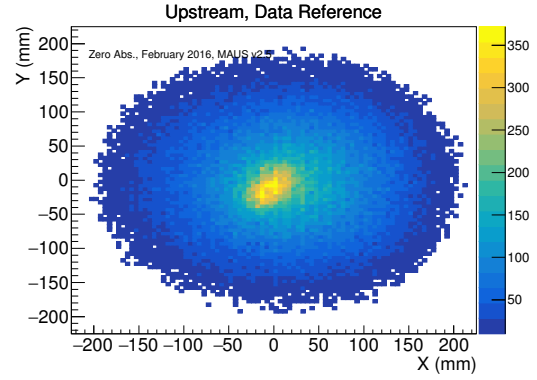


(d) Mean momentum response in simulation

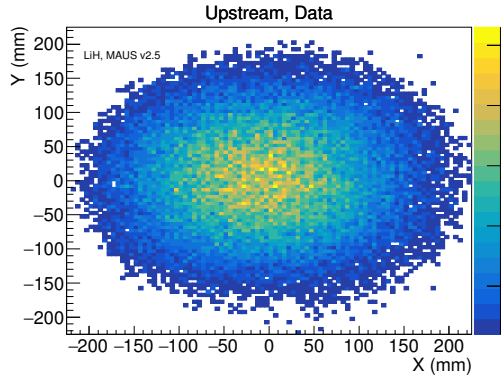
Figure 3: The time of flight and momentum distributions for the three muon beams and the



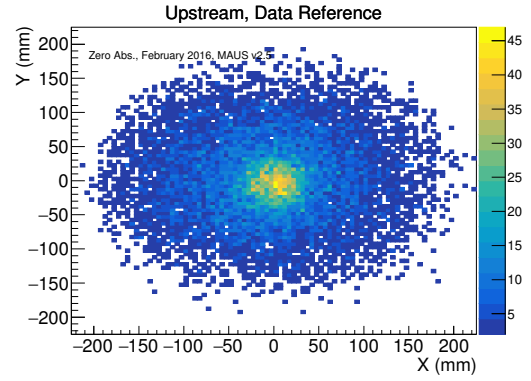
(a) LiH data with US tracks



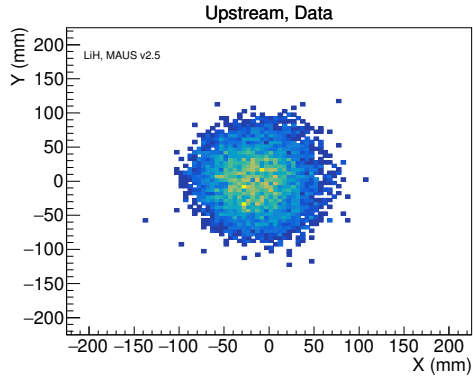
(b) Zero absorber data with US tracks



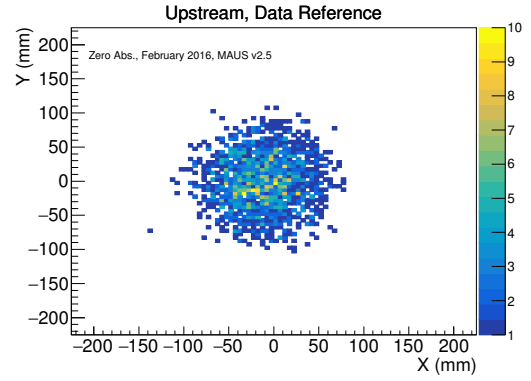
(c) LiH data passing TOF selection



(d) Zero absorber data passing TOF selection

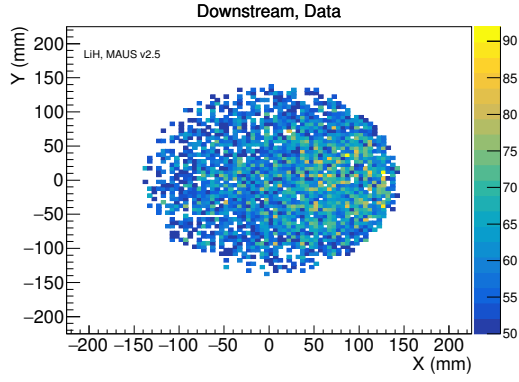


(e) LiH data passing all selections

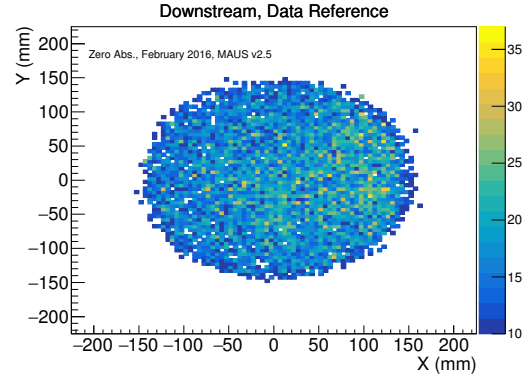


(f) Zero absorber data passing all selections.

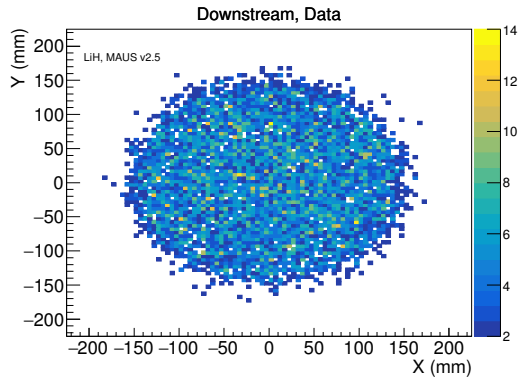
Figure 4: Upstream position distributions for a 200 MeV/c muon beam in the LiH data and the zero absorber beam after particle selection.



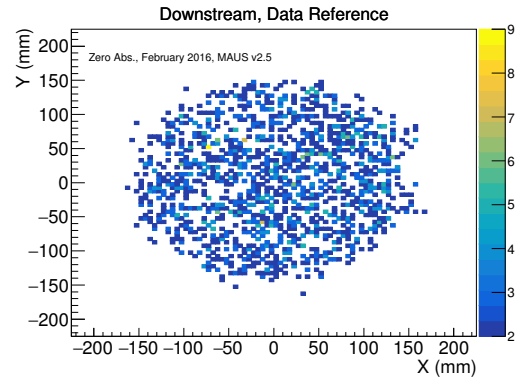
(a) LiH data with US tracks



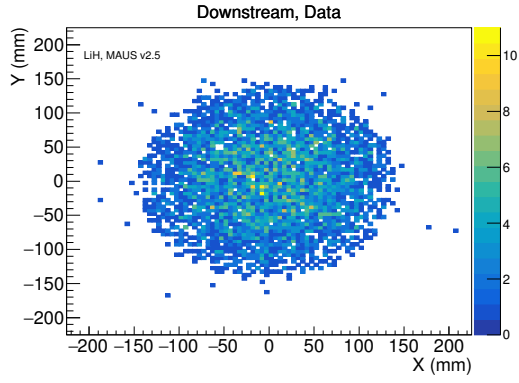
(b) Zero absorber data with US tracks



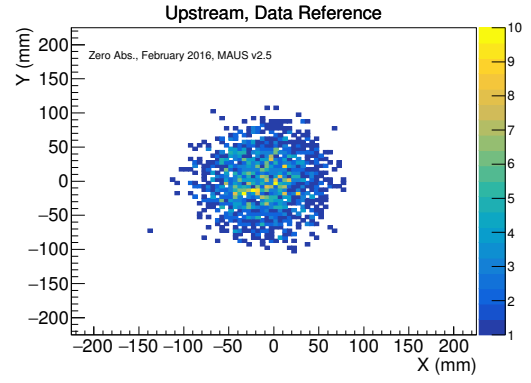
(c) LiH data passing TOF selection



(d) Zero absorber data passing TOF selection

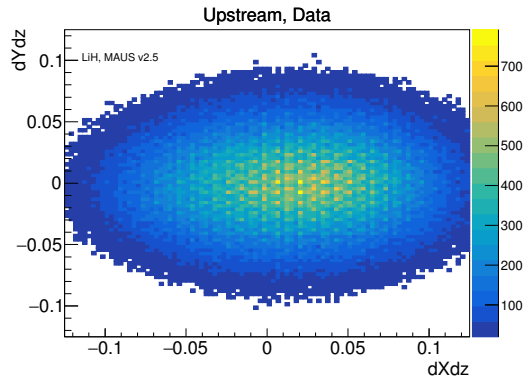


(e) LiH data passing all selections

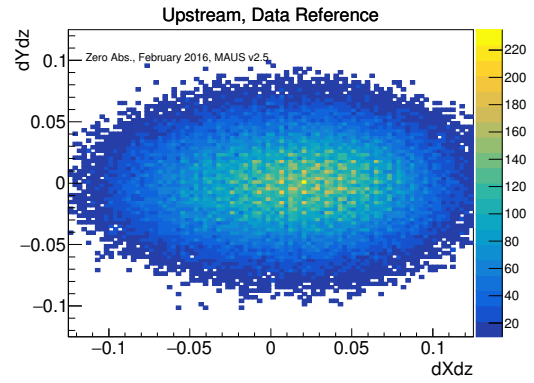


(f) Zero absorber data passing all selections.

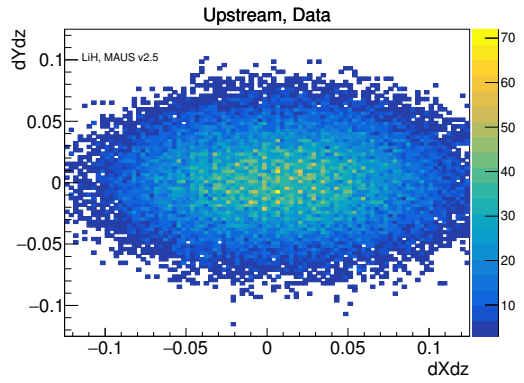
Figure 5: Downstream position distributions for a 200 MeV/c muon beam in the LiH data and the zero absorber beam after particle selection.



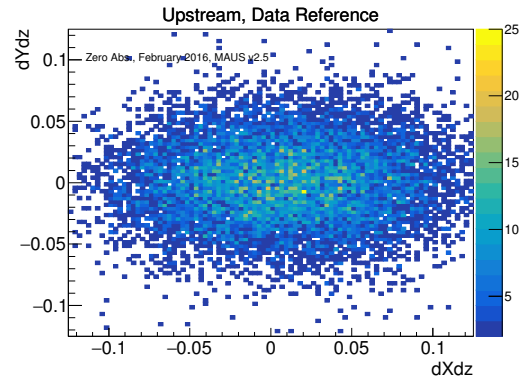
(a) LiH data with US tracks



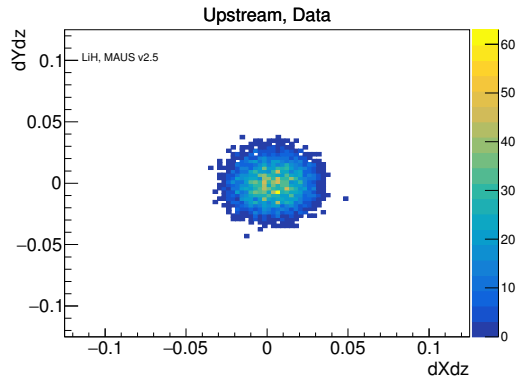
(b) Zero absorber data with US tracks



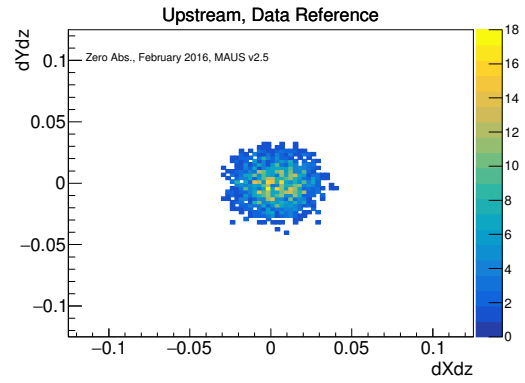
(c) LiH data passing TOF selection



(d) Zero absorber data passing TOF selection

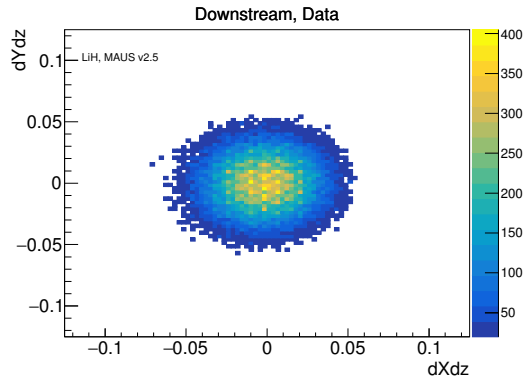


(e) LiH data passing all selections

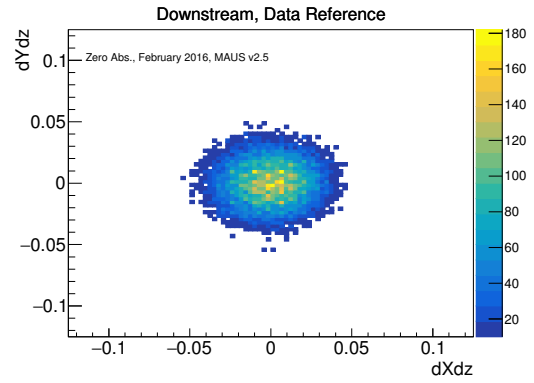


(f) Zero absorber data passing all selections.

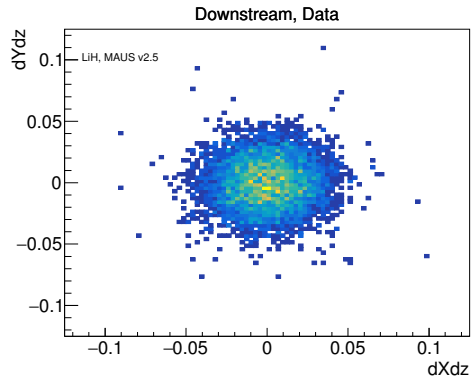
Figure 6: Upstream angle distributions for a 200 MeV/c muon beam in LiH data and the zero absorber beam after particle selection.



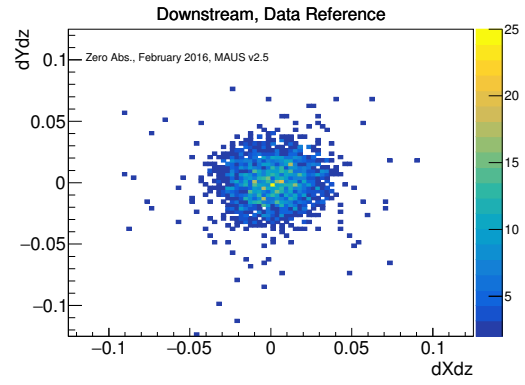
(a) LiH data with US tracks



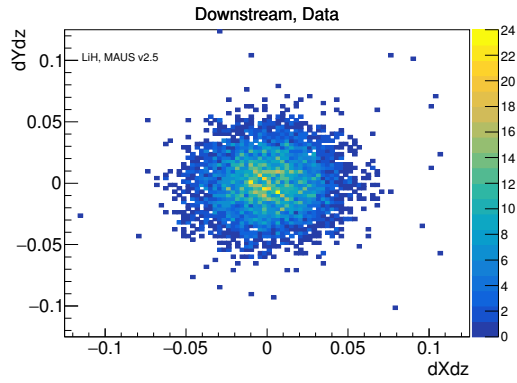
(b) Zero absorber data with US tracks



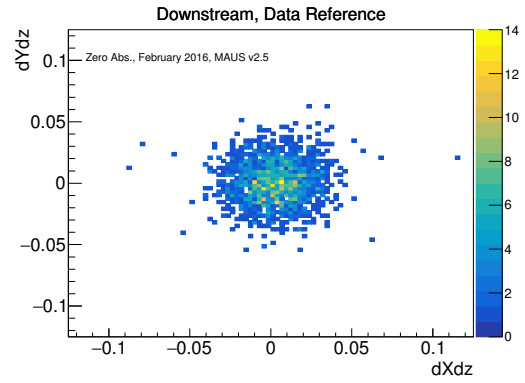
(c) LiH data passing TOF selection



(d) Zero absorber data passing TOF selection

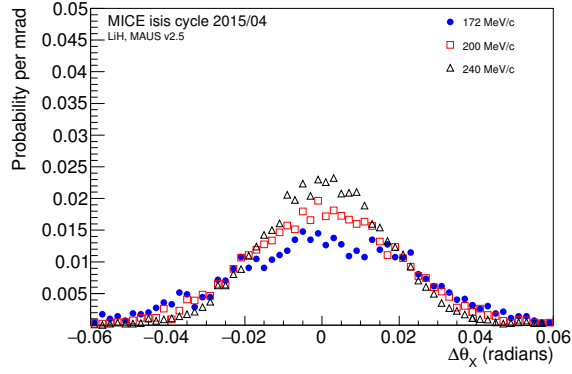


(e) LiH data passing all selections

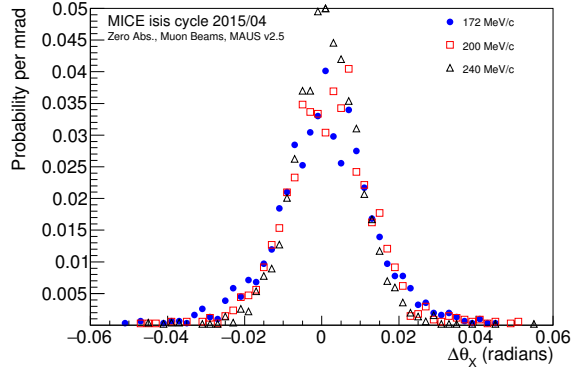


(f) Zero absorber data passing all selections.

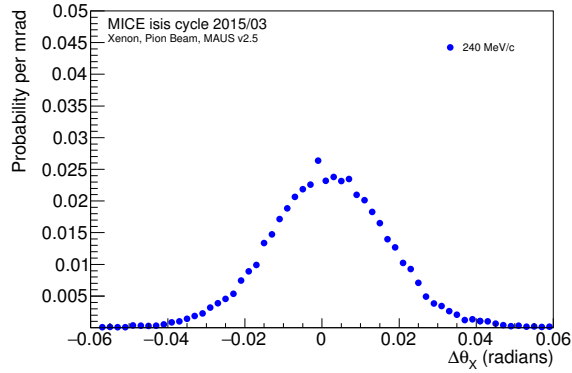
Figure 7: Downstream angle distributions for a 200 MeV/c muon beam in LiH data and the zero absorber beam after particle selection.



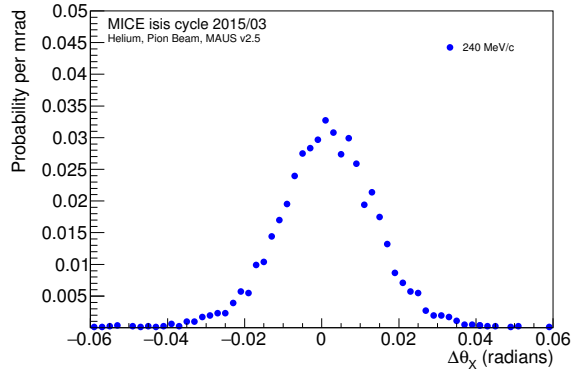
(a) Scattering of μ^+ in LiH



(b) Scattering of μ^+ in null absorber



(c) Scattering of μ^+ in Xenon gas



(d) Scattering of μ^+ in Helium Gas

Figure 8: Measured $\Delta\theta_X$ distributions in the LiH absorber (left) and Zero (right) absorber data sets at the three different momentum settings.

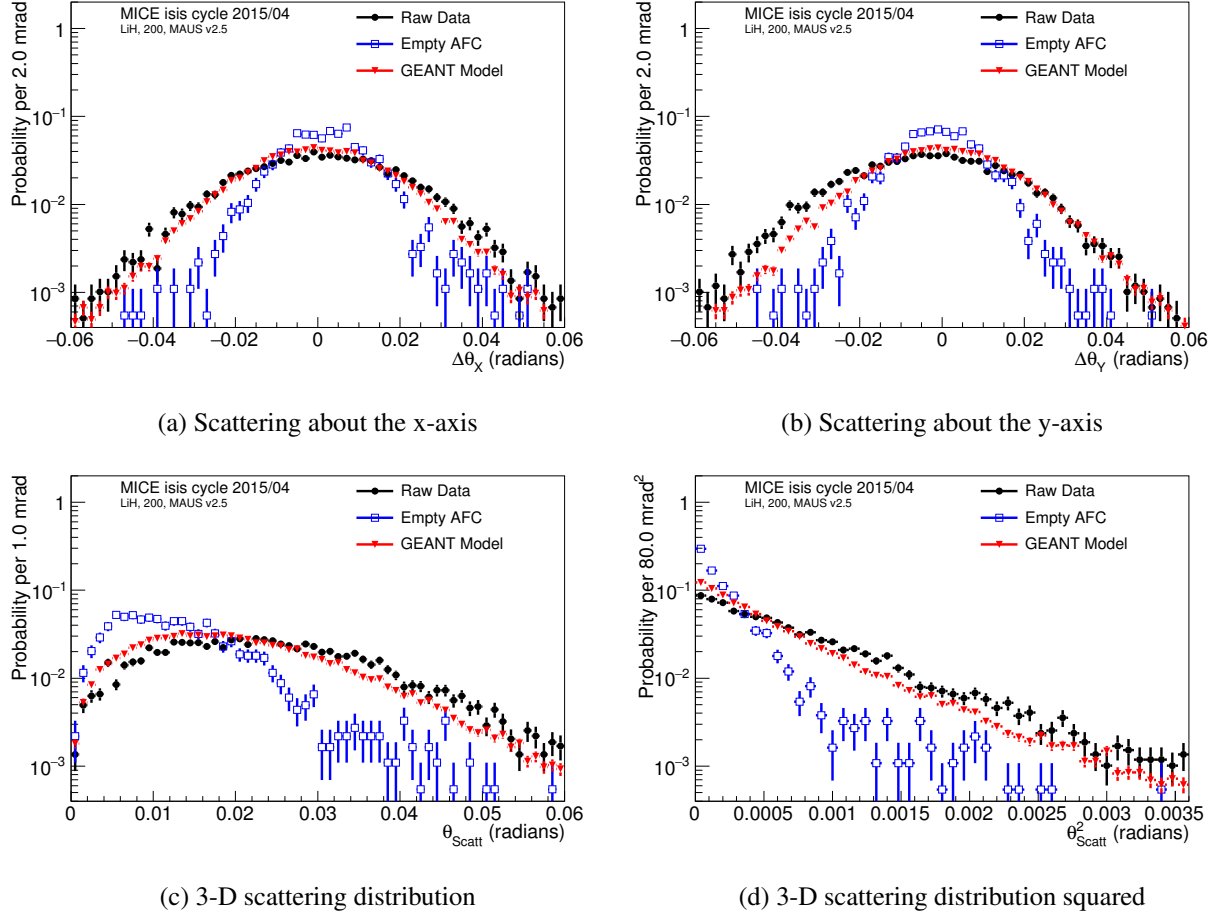


Figure 9: Scattering distributions reconstructed from the 200 MeV/c muon beam with the LiH absorber in place compared to two different scattering models in LiH convolved with the scattering data taken without the LiH absorber in place.

where $n_{\text{data}}(\theta_i^{\text{rec}})$ is the number of events reconstructed at a reconstructed scattering angle (3D or projection angle) contained in the i th bin and $n_{\text{conv}}(\theta_i^{\text{rec}})$ is the number of events in the convolved distribution for the matching bin. The systematic uncertainties are calculated and summed on a bin by bin level. Plots of the reconstructed data with the empty absorber data and simulation of scattering in the absorber are shown in Fig. 9 at 200 MeV/c.

4.2 Deconvolution

The scattering in the absorber material is the physical quantity of interest. To extract this information the effects of scattering in non absorber materials and detector resolution that will appear in the overall scattering measurement must be deconvolved from the required scattering distribution. A deconvolution algorithm using Bayesian statistics[7] has been used based on the implementation contained in the RooUnfold package[8]. This method uses the simulation to provide a probability of observing a given scattering angle from the trackers for a given true scattering angle in the absorber, $P(\Delta\theta_j^{\text{tracker}}|\Delta\theta_i^{\text{abs}})$. This conditional probability is then used to

estimate the number of particles that experience an absorber scattering angle,

$$n(\theta_i^{abs}) = \sum_{j=1}^{n_E} n(\theta_j^{tracker}) P(\theta_i^{abs} | \theta_j^{tracker}), \quad (15)$$

which requires the calculation of the conditional probability

$$P(\theta_i^{abs} | \theta_j^{tracker}) = \frac{P(\theta_j^{tracker} | \theta_i^{abs}) P_0(\theta_i^{abs})}{\sum_{l=1}^{n_c} P(\theta_j^{tracker} | \theta_l^{abs}) P_0(\theta_l^{abs})} \quad (16)$$

The estimate is refined through multiple applications of the algorithm by updating the prior probability by letting $P_0(\theta_i^{abs}) = n(\theta_i^{abs}) / \sum_{i=1}^{n_c} n(\theta_i^{abs})$ in iterations subsequent to the initial calculation in which a flat prior is used. The conditional probability $P(\theta_j^{tracker} | \theta_i^{abs})$ is derived from the convolution where $\theta_j^{tracker}$ is drawn from the sum of the reconstructed scattering angle in the empty absorber data and the scattering angle in the absorber from the convolution model, and θ_i^{abs} is the scattering angle in the absorber alone. When the resulting θ^{abs} distributions are compared with simulation, both the Gaussian width, Θ , and the χ^2 analogous to Eq.14 should be considered.

5 Systematics

Before summarizing the results of the study, the systematic uncertainties will be discussed. Five different contributions to the systematic uncertainty are considered here; the effect of additional material in the scattering model, of variations in the time of flight due to the resolution and momentum calibration, of variations in the measured alignment, and variations in the fiducial radius and angle. The discussions below present the uncertainties in the measured widths with the associated sensitivities using a standardized formulation

$$\sigma_{sys} = \frac{d\Theta}{d\alpha} \approx \frac{\sigma_\alpha}{\Delta\alpha} \Delta\Theta \quad (17)$$

where $\Delta\Theta$ is the change in the distribution width that results from altering a parameter with a known error σ_α in the analysis or simulation by a quantity $\Delta\alpha$. Each of the systematics is defined from the difference imposed by a variation in the named effect multiplied by a scaling factor that represents the uncertainty in the effect divided by the imposed change. The systematics are added on a bin by bin basis to the uncertainties used in the calculation of the χ^2 shown in Section 6 using the same scaling factor. The systematics are reported for three different cases; the projection about the X axis, the projection about the Y axis, and the squared 3-D scattering angle.

5.1 Absorber Material Sensitivity

The thickness of the absorber is an obvious uncertainty in the scattering distribution since the width goes as the square root of the absorber thickness multiplied by the density of the absorber. Measurements of the LiH absorber mass and dimensions yield a density of 0.694 ± 0.003 g/cm³ and based on a 0.254 mm uncertainty in the disk dimensions, including the absorber thickness. Changes in the measurement of the scattering distributions induced by variations in the absorber thickness are modelled by multiplying the widths of the scattering distribution used in the convolution with the empty AFC data by a factor consistent with a 3% density increase. The effect however appears to be negligible given the measured uncertainty with systematic uncertainties less than 10^{-6} .

5.2 Time of Flight and Momentum Sensitivity

A significant systematic uncertainty is due to the TOF selection criteria which directly impacts the momentum range of the particles used in the scattering measurement. The scale is set by the 70 ps resolution of the time of flight measurements. The approximate momentum calibration must also be taken into account. This calibration is taken from the difference between the assumption that the reconstructed momentum is simply offset from the true momentum in the simulation, as shown by the red line in Fig.3d or allowed to systematically scale with momentum. To exaggerate the effect of particles incorrectly appearing inside or outside of the 200 ps selection window, the TOF selection window is offset by ± 400 ps and the difference in the measured scattering width, scaled by a factor of $\sigma_\alpha/\Delta\alpha = 129 \text{ ps}/800 \text{ ps}$, is treated as the systematic uncertainty. The uncertainties shown in Table 4a and 4b indicate that the uncertainties in the momentum are less than 4% of the measured scattering width and with the material systematic, makes up the bulk of the systematic uncertainty.

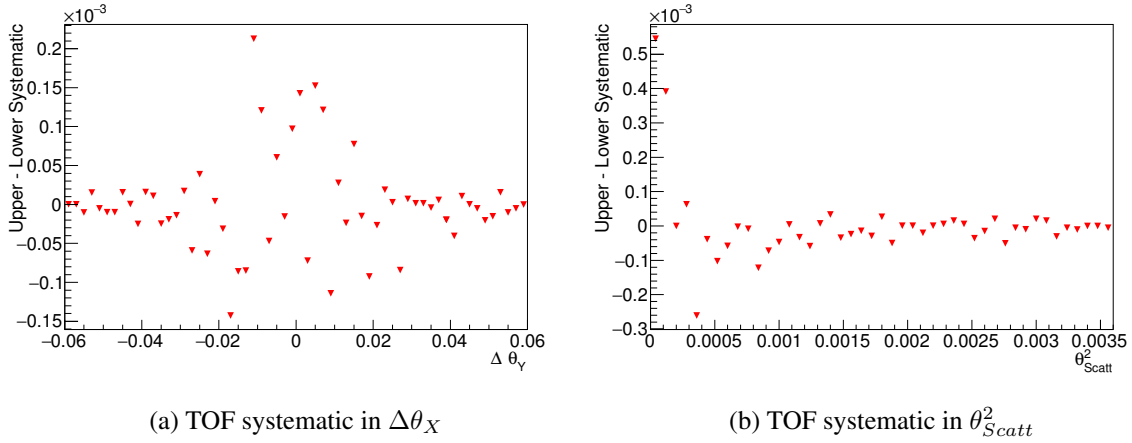


Figure 10: Differences in scattering angles incurred by the systematic extremes used to calculate the time of flight systematic uncertainty.

5.3 Alignment

Uncertainties in the alignment have a direct effect on the angles measured by the tracker. The alignment of the MICE trackers is characterized by four parameters defining offsets, with an uncertainty of 0.2 mm, and angles, with an uncertainty of 0.07 mrad in the X-Z and Y-Z planes; the z position of the tracker and rotations about the z axis are not accessible to the alignment. The alignment of the upstream tracker is independent of the downstream detector inflating the total number of parameters to eight. To assess the effect on the MCS widths, run a number of pseudo experiments have been run which vary the values of all of the alignment parameters within the errors. The uncertainties in the scattering width is extracted from the distributions of the measurements from the pseudo-experiments. After this is complete, the contributed uncertainty from the alignment is at the sub-percent level relative to the scattering width. The contribution has been included in the quoted systematic.

5.4 Fiducial

The choice of the fiducial region may systematically affect the results. A scan over the possible values of the fiducial radius and gradient was completed and the difference between the scattering width of the grid

Table 5: Sensitivity to variations in time of flight determined from offsets of ± 400 ns. Uncertainties are determined assuming a 70 ps TOF detector resolution and a 100 ns momentum calibration uncertainty.

(a) Uncertainties without deconvolution.

Abs.	$\langle p \rangle$	$\Delta\theta_X$			$\Delta\theta_Y$			$\langle\theta_{Scatt}^2\rangle$	
		$\Delta\Theta$ (mrad)	σ_{sys} (mrad)	σ_{sys}/Θ	$\Delta\Theta$ (mrad)	σ_{sys} (mrad)	σ_{sys}/Θ	$\Delta\Theta$ (mrad)	σ_{sys} (mrad)
LiH	172.11 \pm 0.03	-1.7	0.3	0.01	-2.0	0.3	0.01	-3.3	0.3
LiH	199.95 \pm 0.04	-3.5	0.6	0.03	-3.0	0.5	0.03	-3.7	0.6
LiH	239.95 \pm 0.05	-3.2	0.5	0.03	-3.1	0.5	0.03	-4.0	0.5
Xe	240.04 \pm 0.09	-0.3	0.04	0.003	-0.3	0.04	0.003	-0.4	0.04

(b) Uncertainties after deconvolution using GEANT4.

Abs.	$\langle p \rangle$	$\Delta\theta_X$			$\Delta\theta_Y$			$\langle\theta_{Scatt}^2\rangle$		
		$\Delta\Theta$	σ_{sys}	σ_{sys}/Θ	$\Delta\Theta$	σ_{sys}	σ_{sys}/Θ	$\Delta\Theta$	σ_{sys}	σ_{sys}/Θ
LiH	172.11 \pm 0.03	1.3	0.2	0.009	-0.8	0.1	0.006	-1.7	0.3	0.009
LiH	199.95 \pm 0.04	-2.4	0.4	0.02	-3.1	0.5	0.03	-3.5	0.6	0.02
LiH	239.95 \pm 0.05	-3.2	0.5	0.04	-3.2	0.5	0.04	-4.0	0.6	0.03
Xe	240.04 \pm 0.09	-0.03	0.004	0.0006	0.03	0.005	0.0007	-0.5	0.09	0.009

Table 6: Sensitivity to the alignment taken from the maximum variation of the alignment from the generated pseudo experiments

(a) Uncertainties without deconvolution.

Abs.	$\langle p \rangle$	$\Delta\theta_X$			$\Delta\theta_Y$			$\langle\theta_{Scatt}^2\rangle$		
		$\Delta\Theta$	σ_{sys}	σ_{sys}/Θ	$\Delta\Theta$	σ_{sys}	σ_{sys}/Θ	$\Delta\Theta$	σ_{sys}	σ_{sys}/Θ
LiH	172.11 \pm 0.03	-0.01	0.001	6e-05	0.03	0.003	0.0001	-0.01	0.001	4e-05
LiH	199.95 \pm 0.04	-0.008	0.002	9e-05	0.03	0.008	0.0004	-0.02	0.003	0.0001
LiH	239.95 \pm 0.05	0.03	0.005	0.0003	-0.03	0.006	0.0003	0.04	0.008	0.0003
Xe	240.04 \pm 0.09	0.64	0.05	0.0	0.55	0.05	0.0	0.88	0.07	0.0

(b) Uncertainties after deconvolution using GEANT4.

Abs.	$\langle p \rangle$	$\Delta\theta_X$			$\Delta\theta_Y$			$\langle\theta_{Scatt}^2\rangle$		
		$\Delta\Theta$	σ_{sys}	σ_{sys}/Θ	$\Delta\Theta$	σ_{sys}	σ_{sys}/Θ	$\Delta\Theta$	σ_{sys}	σ_{sys}/Θ
LiH	172.11 \pm 0.03	-0.04	0.005	0.0002	0.2	0.03	0.001	-0.5	0.06	0.002
LiH	199.95 \pm 0.04	-0.1	0.03	0.002	0.07	0.02	0.0009	0.05	0.01	0.0005
LiH	239.95 \pm 0.05	0.004	0.0007	5e-05	0.06	0.01	0.0008	0.03	0.006	0.0003
Xe	240.04 \pm 0.09	0.34	0.01	0.0	0.36	0.02	0.0	1.72	0.1	0.01

points adjacent to the selection values of 150 mm and 12 mrad are used to set the uncertainty with a scaling factor based on the uncertainties in position and angle which are 0.495 mm and 0.56 mrad respectively. The differences measured from changes in the fiducial gradient are then scaled by 0.56 mrad/10 mrad = 0.056, and the differences measured from changes in the fiducial radius are scaled by 0.495 mm/20 mm = 0.0248 to get the systematic uncertainties for the fiducial selection. The scattering width is insensitive to the radial fiducial selection with systematic uncertainties on the sub-percent level. In contrast the gradient used in the fiducial selection has a larger effect, approaching 1% for the deconvolved results.

Table 7: Sensitivities to changes in the fiducial gradient assuming a fixed radial selection of 150 mm.

(a) Uncertainties without deconvolution.

Abs.	$\langle p \rangle$	$\Delta\theta_X$			$\Delta\theta_Y$			$\langle\theta_{Scatt}^2\rangle$		
		$\Delta\Theta$	σ_{sys}	σ_{sys}/Θ	$\Delta\Theta$	σ_{sys}	σ_{sys}/Θ	$\Delta\Theta$	σ_{sys}	σ_{sys}/Θ
LiH	172.11 \pm 0.03	0.3	0.01	0.0006	-0.3	0.02	0.0007	0.1	0.005	0.0002
LiH	199.95 \pm 0.04	0.3	0.01	0.0007	0.3	0.02	0.0009	0.3	0.01	0.0005
LiH	239.95 \pm 0.05	0.07	0.004	0.0002	0.2	0.01	0.0007	0.1	0.006	0.0003
Xe	240.04 \pm 0.09	0.5	0.02	0.002	0.4	0.02	0.001	0.7	0.03	0.002

(b) Uncertainties after deconvolution using GEANT4.

Abs.	$\langle p \rangle$	$\Delta\theta_X$			$\Delta\theta_Y$			$\langle\theta_{Scatt}^2\rangle$		
		$\Delta\Theta$	σ_{sys}	σ_{sys}/Θ	$\Delta\Theta$	σ_{sys}	σ_{sys}/Θ	$\Delta\Theta$	σ_{sys}	σ_{sys}/Θ
LiH	172.11 \pm 0.03	-0.4	0.02	0.0009	-1.5	0.07	0.003	-1.3	0.06	0.002
LiH	199.95 \pm 0.04	-1.0	0.05	0.003	-1.3	0.07	0.004	-1.2	0.06	0.002
LiH	239.95 \pm 0.05	-0.9	0.04	0.003	-0.7	0.03	0.002	-1.1	0.05	0.003
Xe	240.04 \pm 0.09	-0.3	0.01	0.002	-0.3	0.01	0.002	-0.8	0.04	0.004

6 Results

The residuals between the data and the two models under consideration appear in Fig. 12. The χ^2 derived from these residuals appear in Table 8. The χ^2 was calculated assuming 40 data points so some of the distributions collected show remarkable agreement with data.

The Bayes deconvolution has been applied to the collected data sets using the forward convolution of the GEANT4 and CCM implementations of scattering in the LiH absorber to provide the conditional probability necessary for the deconvolution. The raw and deconvolved data taken with the 200 MeV/c beam are shown in Fig. 13 assuming a GEANT4 LiH simulation. There is very little difference between the GEANT4 simulation and the Carlisle-Cobb simulations, and the deconvolved results are identical for the two results in LiH.

The fluctuations dominate the processed distribution at angles greater than 45 milliradians for all three data sets as shown in Fig. 8. The distributions of the projections in X and Y were characterized using a Gaussian fit within this range, with the results shown in Table 9 for data and simulation. In contrast the squared scattering angle is characterized by the mean of the angles less than 36 mrad². The table shows that the YZ and XZ projections of the scattering distributions have consistent widths demonstrating that the fiducial selection reduces the asymmetry within the data.

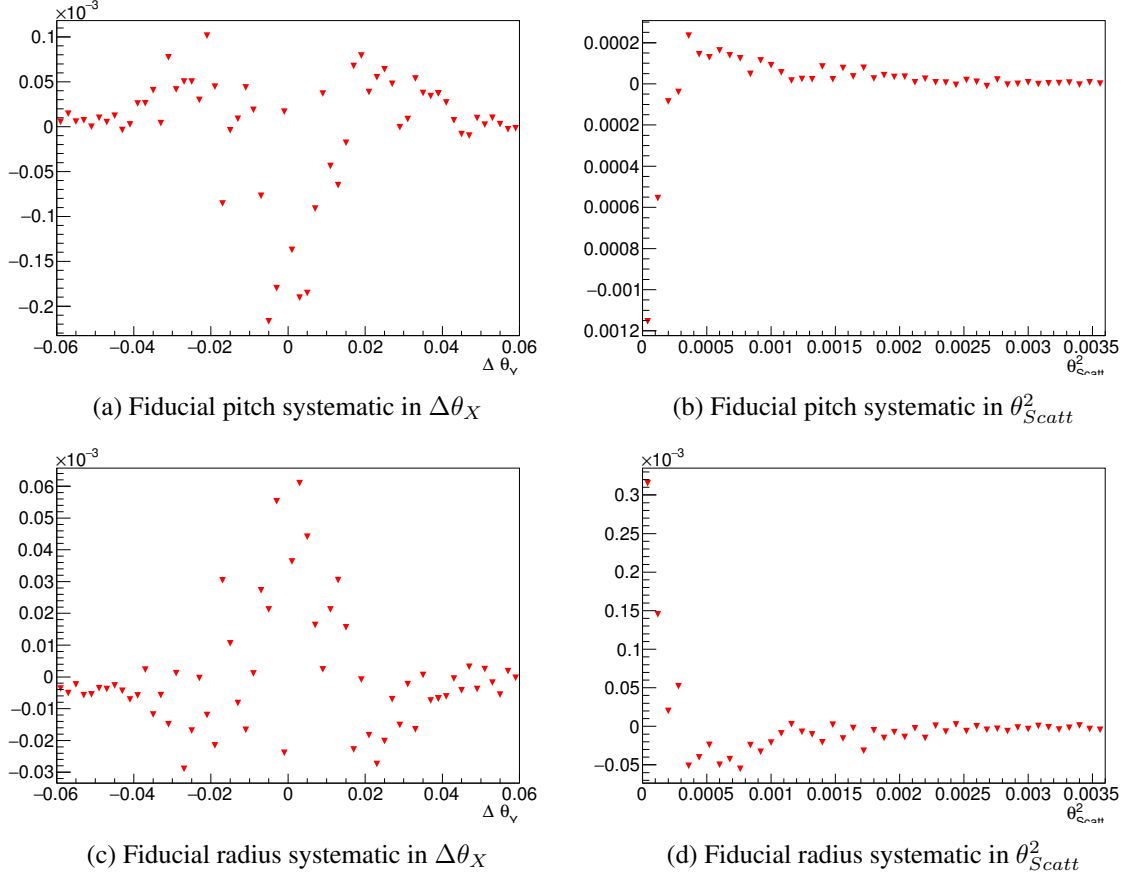


Figure 11: Differences in scattering angles incurred by the systematic extremes used to calculate the fiducial systematic uncertainties.

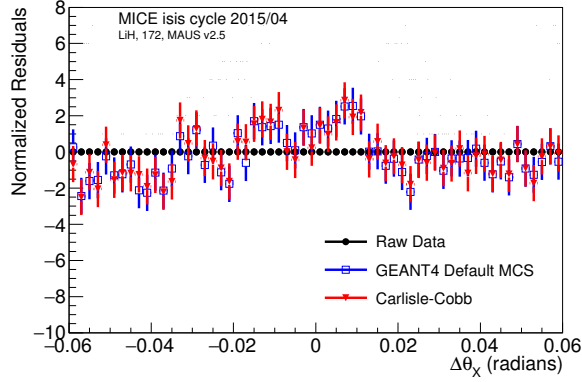
Table 8: Sensitivities to changes in the fiducial radial selection assuming a fiducial gradient of 12 mrad.

(a) Uncertainties without deconvolution.

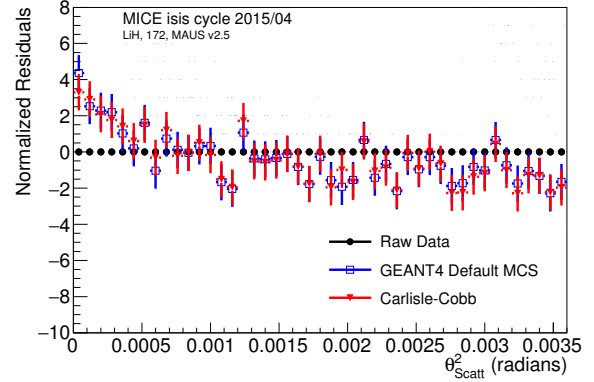
Abs.	$\langle p \rangle$	$\Delta\theta_X$			$\Delta\theta_Y$			$\langle \theta_{Scatt}^2 \rangle$		
		$\Delta\Theta$	σ_{sys}	σ_{sys}/Θ	$\Delta\Theta$	σ_{sys}	σ_{sys}/Θ	$\Delta\Theta$	σ_{sys}	σ_{sys}/Θ
LiH	172.11 ± 0.03	0.3	0.008	0.0003	0.09	0.002	9e-05	0.01	0.0003	0.0
LiH	199.95 ± 0.04	-0.2	0.006	0.0003	-0.2	0.005	0.0002	-0.1	0.003	0.0001
LiH	239.95 ± 0.05	-0.006	0.0001	0.0	-0.1	0.003	0.0002	-0.06	0.001	6e-05
Xe	240.04 ± 0.09	-0.3	0.008	0.0006	-0.2	0.005	0.0004	-0.4	0.01	0.0005

(b) Uncertainties after deconvolution using GEANT4.

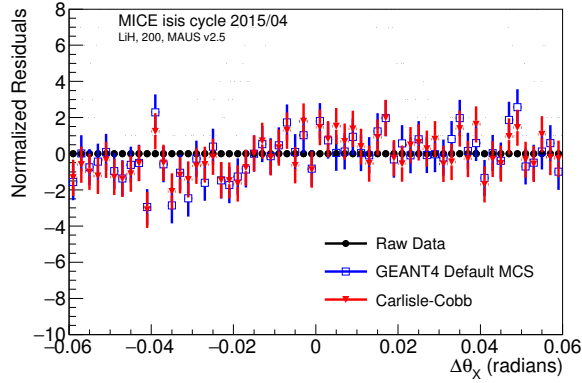
Abs.	$\langle p \rangle$	$\Delta\theta_X$			$\Delta\theta_Y$			$\langle \theta_{Scatt}^2 \rangle$		
		$\Delta\Theta$	σ_{sys}	σ_{sys}/Θ	$\Delta\Theta$	σ_{sys}	σ_{sys}/Θ	$\Delta\Theta$	σ_{sys}	σ_{sys}/Θ
LiH	172.11 ± 0.03	1.6	0.04	0.002	3.1	0.07	0.003	1.3	0.03	0.001
LiH	199.95 ± 0.04	1.3	0.03	0.002	0.9	0.02	0.001	1.1	0.03	0.001
LiH	239.95 ± 0.05	0.9	0.02	0.001	0.9	0.02	0.001	0.9	0.02	0.001
Xe	240.04 ± 0.09	0.2	0.005	0.0008	0.2	0.006	0.0009	1.4	0.03	0.003



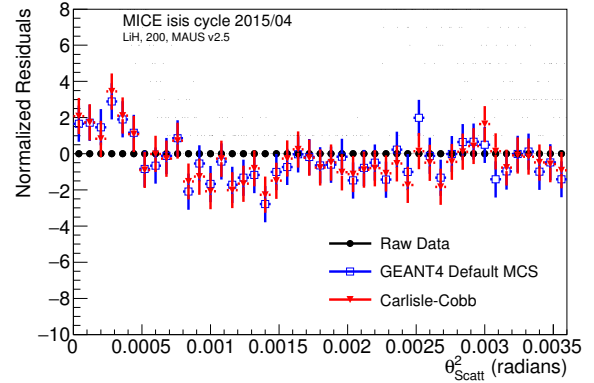
(a) Scattering about X-axis at 172 MeV/c



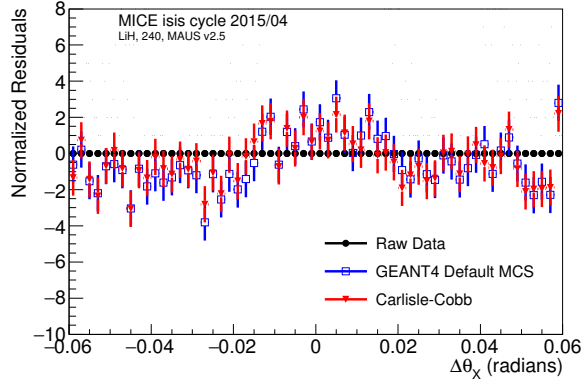
(b) Squared 3-D scattering angles at 172 MeV/c



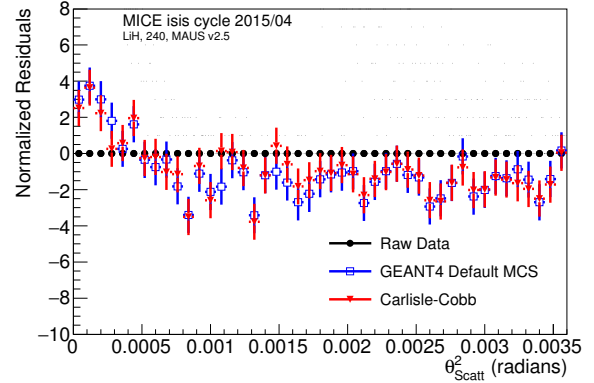
(c) Scattering about X-axis at 200 MeV/c



(d) Squared 3-D scattering angles at 200 MeV/c



(e) Scattering about X-axis at 240 MeV/c



(f) Squared 3-D scattering angles at 240 MeV/c

Figure 12: Scattering residuals between data from a muon beam with the LiH absorber in place compared to two different scattering models in LiH convolved with the scattering data taken without the LiH absorber in place.

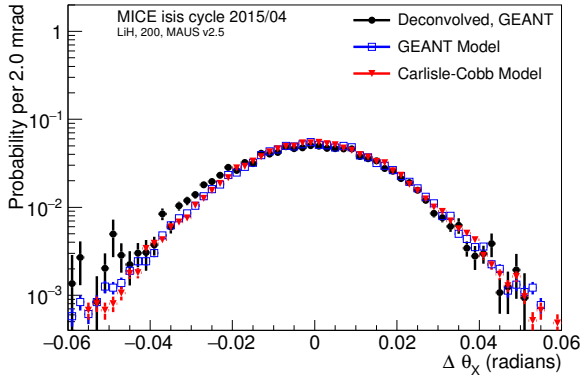
Table 9: Measurements of distribution widths and the χ^2 comparisons between data and two different implementations of multiple scattering. The χ^2 were calculated using 100 degrees of freedom. Statistical uncertainties alone have been given.

(a) Measurements in Lithium Hydride

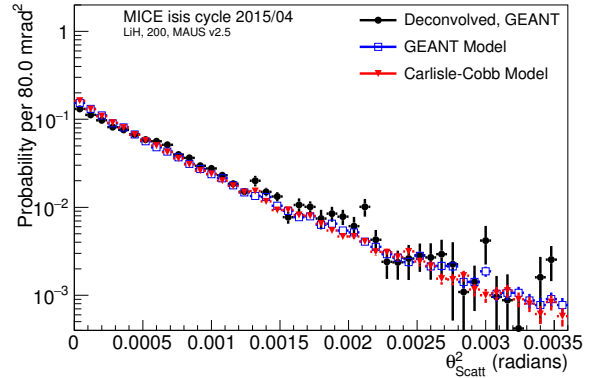
p	Angle	Θ_{Data} (mrad)	Θ_{G4} (mrad)	χ^2	Θ_{CC} (mrad)	χ^2
172.11 \pm 0.03	$\Delta\theta_X$	23.19 \pm 0.52 \pm 0.28	20.67 \pm 0.14	71.4 / 45	20.95 \pm 0.14	70.7 / 45
172.11 \pm 0.03	$\Delta\theta_Y$	23.77 \pm 0.56 \pm 0.34	20.95 \pm 0.14	98.4 / 45	21.15 \pm 0.14	95.1 / 45
199.95 \pm 0.04	$\Delta\theta_X$	18.96 \pm 0.24 \pm 0.57	18.37 \pm 0.1	62.7 / 45	18.26 \pm 0.1	56.6 / 45
199.95 \pm 0.04	$\Delta\theta_Y$	19.12 \pm 0.25 \pm 0.49	18.18 \pm 0.1	93.0 / 45	18.06 \pm 0.1	92.6 / 45
239.95 \pm 0.05	$\Delta\theta_X$	16.03 \pm 0.13 \pm 0.52	15.04 \pm 0.06	88.3 / 45	15.27 \pm 0.06	58.1 / 45
239.95 \pm 0.05	$\Delta\theta_Y$	15.91 \pm 0.14 \pm 0.5	14.89 \pm 0.06	190.1 / 45	15.02 \pm 0.06	130.1 / 45
p		$\sqrt{\langle\theta_{Scatt}^2\rangle_{G4}^{meas}}$ (mrad)	$\sqrt{\langle\theta_{Scatt}^2\rangle_{G4}^{true}}$	χ^2	$\sqrt{\langle\theta_{Scatt}^2\rangle_{CC}^{true}}$	χ^2
172.11 \pm 0.03		33.23 \pm 1.43 \pm 0.53	29.52 \pm 0.35	93.2 / 46	29.8 \pm 0.36	93.8 / 46
199.95 \pm 0.04		27.24 \pm 0.59 \pm 0.6	25.72 \pm 0.23	65.0 / 46	25.6 \pm 0.22	66.6 / 46
239.95 \pm 0.05		22.51 \pm 0.29 \pm 0.65	21.13 \pm 0.12	150.8 / 46	21.44 \pm 0.12	130.8 / 46

(b) Measurements in Xenon

p	Angle	Θ_{Data} (mrad)	Θ_{G4} (mrad)	χ^2	Θ_{CC} (mrad)	χ^2
240.04 \pm 0.09	$\Delta\theta_X$	13.95 \pm 0.16 \pm 0.04	14.5 \pm 0.11	17.1 / 45	16.0 \pm 0.1	55.5 / 45
240.04 \pm 0.09	$\Delta\theta_Y$	14.15 \pm 0.18 \pm 0.04	14.14 \pm 0.11	22.6 / 45	15.95 \pm 0.1	47.7 / 45
p		$\sqrt{\langle\theta_{Scatt}^2\rangle_{G4}^{meas}}$ (mrad)	$\sqrt{\langle\theta_{Scatt}^2\rangle_{G4}^{true}}$	χ^2	$\sqrt{\langle\theta_{Scatt}^2\rangle_{CC}^{true}}$	χ^2
240.04 \pm 0.09		19.75 \pm 0.35 \pm 0.06	20.24 \pm 0.23	286.5 / 46	22.46 \pm 0.22	297.0 / 46



(a) Scattering about X-axis



(b) 3D scattering angle

Figure 13: Projected and 3D scattering distributions at 200 MeV/c before and after deconvolution using the GEANT scattering model to provide the response distribution. The GEANT scattering distribution in the lithium hydride distribution is provided for comparison.

Table 10: Measurements of distribution widths and χ^2 between the data after deconvolution of spectra using GEANT4 to provide the absorber scattering response and the scattering models.

(a) Measurements in Lithium Hydride with a deconvolution using a GEANT4 scattering simulation

p	Angle	Θ_{G4}^{meas} (mrad)	Θ_{G4}^{true} (mrad)	χ^2	Θ_{CC}^{true} (mrad)	χ^2
172.11±0.03	$\Delta\theta_X$	22.46±0.34±0.23	19.28±0.11	229.0 / 45	19.55±0.11	226.7 / 45
172.11±0.03	$\Delta\theta_Y$	22.59±0.36±0.39	19.06±0.1	294.4 / 45	19.47±0.11	316.8 / 45
199.95±0.04	$\Delta\theta_X$	17.13±0.14±0.45	16.55±0.08	119.5 / 45	16.42±0.08	164.0 / 45
199.95±0.04	$\Delta\theta_Y$	17.41±0.14±0.59	16.41±0.08	254.1 / 45	16.3±0.08	278.2 / 45
239.95±0.05	$\Delta\theta_X$	14.46±0.07±0.56	13.38±0.05	276.8 / 45	13.61±0.05	270.6 / 45
239.95±0.05	$\Delta\theta_Y$	14.12±0.08±0.55	13.29±0.05	625.8 / 45	13.52±0.05	439.4 / 45
p		$\sqrt{\langle\theta_{Scatt}^2\rangle_{G4}^{meas}}$ (mrad)	$\sqrt{\langle\theta_{Scatt}^2\rangle_{G4}^{true}}$	χ^2	$\sqrt{\langle\theta_{Scatt}^2\rangle_{CC}^{true}}$	χ^2
172.11±0.03		31.63±0.84±0.41	26.78±0.25	331.2 / 46	27.38±0.26	309.7 / 46
199.95±0.04		24.8±0.35±0.64	23.17±0.17	129.8 / 46	22.94±0.17	147.6 / 46
239.95±0.05		20.37±0.17±0.69	18.85±0.1	333.5 / 46	19.19±0.1	266.2 / 46

(b) Measurements in Xenon with a deconvolution using a GEANT4 scattering simulation

p	Angle	Θ_{G4}^{meas} (mrad)	Θ_{G4}^{true} (mrad)	χ^2	Θ_{CC}^{true} (mrad)	χ^2
240.04±0.09	$\Delta\theta_X$	6.34±0.06±0.0	6.73±0.06	268.7 / 45	12.08±0.07	2395.4 / 45
240.04±0.09	$\Delta\theta_Y$	6.55±0.07±0.0	6.72±0.06	222.6 / 45	12.04±0.07	1985.5 / 45
p		$\sqrt{\langle\theta_{Scatt}^2\rangle_{G4}^{meas}}$ (mrad)	$\sqrt{\langle\theta_{Scatt}^2\rangle_{G4}^{true}}$	χ^2	$\sqrt{\langle\theta_{Scatt}^2\rangle_{CC}^{true}}$	χ^2
240.04±0.09		9.93±0.17±0.09	10.19±0.15	289.0 / 46	17.1±0.15	2822.3 / 46

(c) Measurements in Lithium Hydride with a deconvolution using a Carlisle-Cobb scattering simulation

p	Angle	Θ_{CC}^{meas} (mrad)	Θ_{G4}^{true} (mrad)	χ^2	Θ_{CC}^{true} (mrad)	χ^2
172.11±0.03	$\Delta\theta_X$	22.14±0.34±0.39	19.28±0.11	227.9 / 45	19.55±0.11	201.6 / 45
172.11±0.03	$\Delta\theta_Y$	22.51±0.36±0.5	19.06±0.1	350.0 / 45	19.47±0.11	292.0 / 45
199.95±0.04	$\Delta\theta_X$	17.22±0.15±0.51	16.55±0.08	125.6 / 45	16.42±0.08	99.2 / 45
199.95±0.04	$\Delta\theta_Y$	17.36±0.15±0.53	16.41±0.08	257.8 / 45	16.3±0.08	230.6 / 45
239.95±0.05	$\Delta\theta_X$	14.47±0.08±0.55	13.38±0.05	303.0 / 45	13.61±0.05	193.3 / 45
239.95±0.05	$\Delta\theta_Y$	14.13±0.08±0.57	13.29±0.05	719.5 / 45	13.52±0.05	396.3 / 45
p		$\sqrt{\langle\theta_{Scatt}^2\rangle_{CC}^{meas}}$ (mrad)	$\sqrt{\langle\theta_{Scatt}^2\rangle_{G4}^{true}}$	χ^2	$\sqrt{\langle\theta_{Scatt}^2\rangle_{CC}^{true}}$	χ^2
172.11±0.03		31.78±0.88±0.46	26.78±0.25	320.8 / 46	27.38±0.26	294.2 / 46
199.95±0.04		24.73±0.36±0.6	23.17±0.17	136.4 / 46	22.94±0.17	144.1 / 46
239.95±0.05		20.19±0.16±0.62	18.85±0.1	294.7 / 46	19.19±0.1	234.3 / 46

(d) Measurements in Xenon with a deconvolution using a Carlisle-Cobb scattering simulation

p	Angle	Θ_{G4}^{meas} (mrad)	Θ_{G4}^{true} (mrad)	χ^2	Θ_{CC}^{true} (mrad)	χ^2
240.04±0.09	$\Delta\theta_X$	9.73±0.06±0.02	6.73±0.06	1711.7 / 45	12.08±0.07	576.3 / 45
240.04±0.09	$\Delta\theta_Y$	9.87±0.07±0.02	6.72±0.06	1610.9 / 45	12.04±0.07	436.6 / 45
p		$\sqrt{\langle\theta_{Scatt}^2\rangle_{CC}^{meas}}$ (mrad)	$\sqrt{\langle\theta_{Scatt}^2\rangle_{G4}^{true}}$	χ^2	$\sqrt{\langle\theta_{Scatt}^2\rangle_{CC}^{true}}$	χ^2
240.04±0.09		14.04±0.15±0.05	10.19±0.15	2406.2 / 46	17.1±0.15	822.4 / 46

6.1 Xenon Analyses

There is a significant difference between the two models for the Xenon data which must be addressed. The GEANT4 simulation shows large tails which appear in neither the data or the Carlisle-Cobb simulation. The GEANT simulation is shown in Fig. 14a with data while the Carlisle-Cobb simulation is shown with the data in Fig. 14b. However, both the comparison of the raw data to the convolved simulations and the deconvolved scattering distribution widths indicate a preference for the GEANT4 simulation. The relative width of the Carlisle-Cobb simulation to that of GEANT4 is consistent with an increase in the Xenon density by a factor of 3.4. The residuals between the raw distributions and the simulations are shown in Fig. 14e while those between the deconvolved distributions and the simulations are shown in Fig. 14f

7 Momentum Dependent Measurements

The muon beam data affords a unique opportunity to measure the momentum dependence of the multiple scattering because of the wide momentum distribution. By using the machinery developed to optimize the time of flight selection the widths of the scattering distribution can be determined for each TOF bin, which may be plotted as a function of momentum to confirm the functional representation of the scattering. Each bin is subject to the same analysis as that used in to test the nominal scattering momenta. The integral of the events contained in each TOF bin are shown as a function of the mean momentum in Fig. 15a. Only bins with more than 2000 events are used in the analysis. The deconvolved scattering widths as a function of momentum, shown in Fig 15b to 15d, is fit to a $1/p\beta$ dependence motivated by Equation 10. In that case, the coefficient of the momentum dependent term should be $13.6 \text{ MeV/c} \sqrt{\frac{z}{X_0}} \left(1 + 0.0038 \ln \frac{z}{X_0}\right)$. The offset should be consistent with zero.

The parameters resulting from this fit are shown in the above figures with the upper and lower limits. The values determined from the fits are shown in Table 10. The systematic uncertainty associated with the momentum scale is included in the errors shown in the figures, which were assessed by using the results of the fits with statistical uncertainties only to provide an estimate of the derivative of Θ with respect to momentum prior and then to relate the time of flight uncertainty to the momentum i.e.

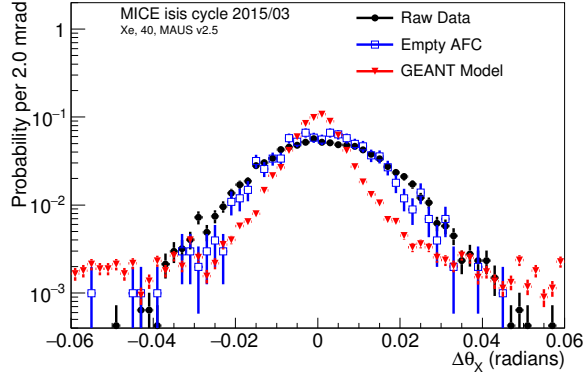
$$\sigma_{\Theta} = \frac{d\Theta}{dp} \frac{dp}{dt_{TOF}} \sigma_{TOF} = \frac{\Theta(p + 4 \text{ MeV/c}) - \Theta(p - 4 \text{ MeV/c})}{8 \text{ MeV/c}} \frac{a}{(t_{TOF} - b)^2} \sigma_{TOF} \quad (18)$$

where a and b are provided by the fit to Fig. 3b ($a = 1043 \pm 31 \text{ ns} \cdot \text{MeV/c}$ and $b = 23.2 \pm 0.2 \text{ ns}$) and $\sigma_{TOF} = 129 \text{ ns}$ as defined for the time of flight systematic. With these errors included in the error bars on the data points the fitted uncertainty (the limits of which are give by the blue lines in the figures) also include the systematic uncertainties.

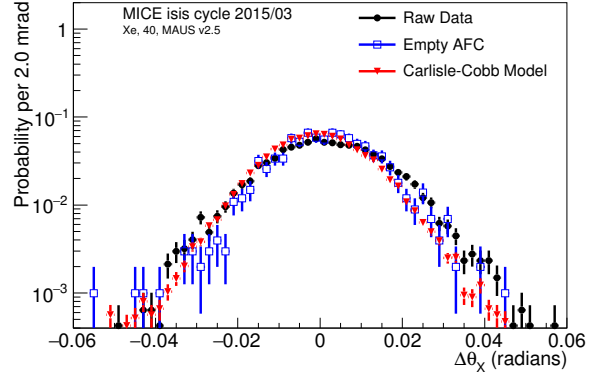
Measurements using the projected angles are systematically less than the PDG prediction as shown in Fig 15b and Fig 15c. The root mean square scattering angle is consistent with the PDG prediction. The predictions given by GEANT are also shown in the figures, indicating an underestimate of the scattering relative to the PDG formula and the reported data, especially at low momenta. The momentum dependence of GEANT is also not as strong as that of the data.

8 Conclusion

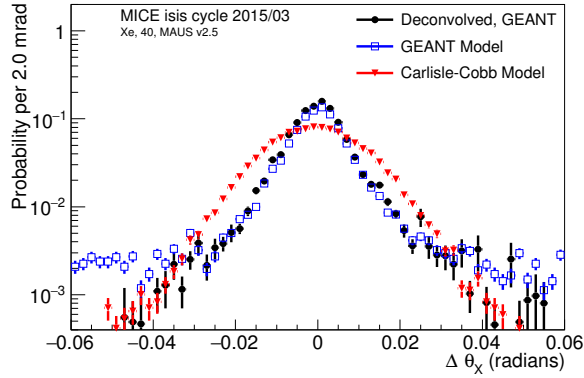
Presented here is an analysis of the LiH scattering data compiled over ISIS user run 2015/04 and the Xenon scattering data compiled over user run 2015/03. These data were compared to different implementations of the



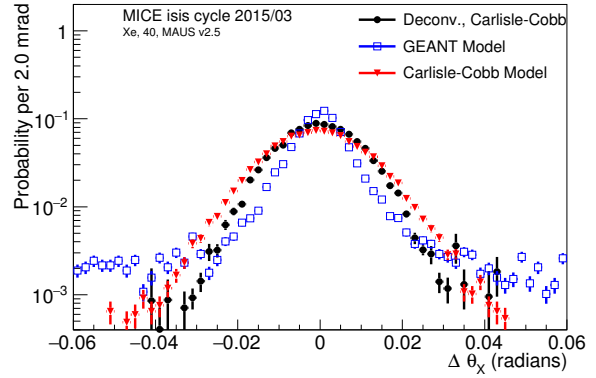
(a) Raw data compared with GEANT4



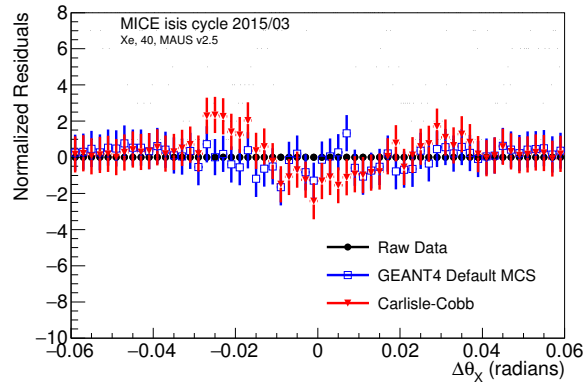
(b) Raw data compared with CC simulation



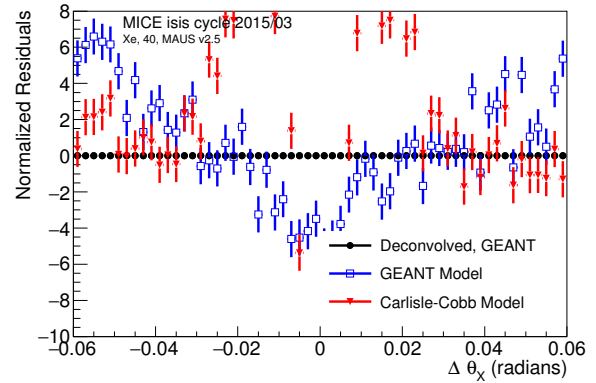
(c) Deconvolved data compared with GEANT4



(d) Deconvolved data compared with CC simulation

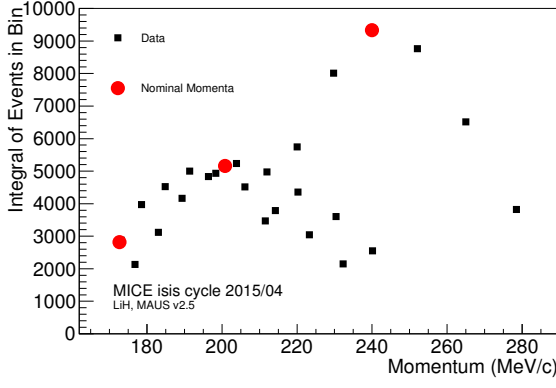


(e) Residuals between the raw data and simulations.

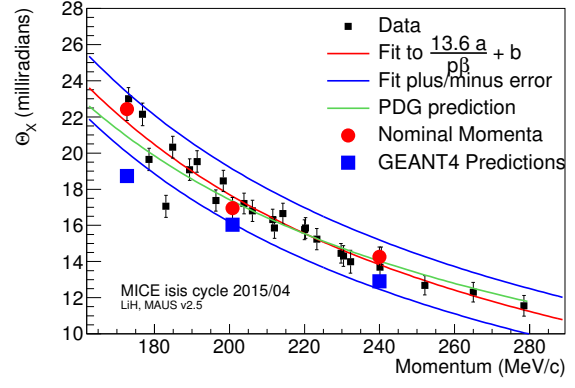


(f) Residuals between the data with a GEANT deconvolution and the simulations.

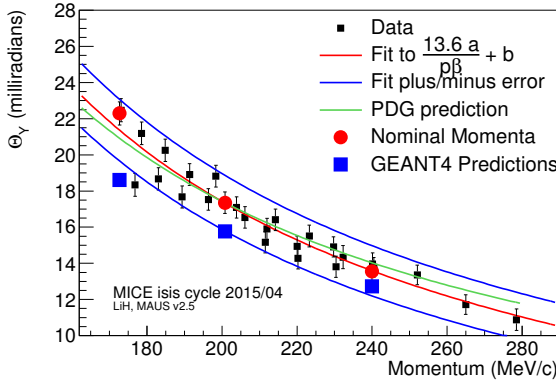
Figure 14: Projected scattering distributions about the X-axis and residuals due to interactions in Xenon.



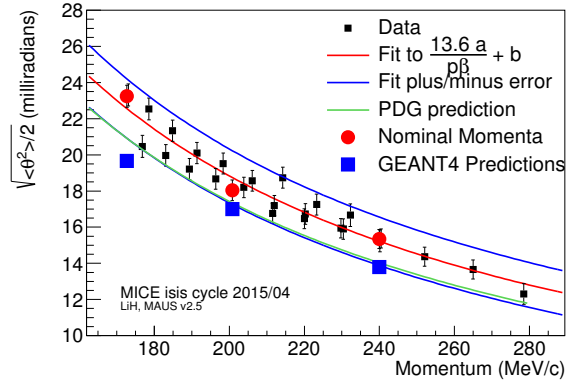
(a) Number of events in TOF bins



(b) Width in scattering angle $\Delta\theta_X$.



(c) Width in scattering angle $\Delta\theta_Y$



(d) Square root of mean square scattering angle

Figure 15: The results of the scattering analysis using data from all three nominal beam settings. Scattering widths are reported after application of deconvolution.

multiple scattering in lithium hydride; the compact implementation used as the GEANT default and a more exact implementation proposed in Tim Carlisle's thesis. A χ^2 statistic was used to make qualitative statements about the validity of the proposed models. The two implementations, when using consistent central momenta, produce consistent results for the LiH disk. A deconvolution procedure was then applied to the data with the same conclusion. Widths from the scattering distributions projected onto the X-Z and Y-Z planes produce consistent results given the uncertainties. The scattering measurements can be taken from $\sqrt{\langle\theta_{scatt}^2\rangle}/2$ so that $\Theta = 22.4 \pm 0.6 \pm 0.3$ mrad at 172 MeV/c, $\Theta = 17.5 \pm 0.3 \pm 0.4$ mrad at 200 MeV/c, and $\Theta = 14.4 \pm 0.1 \pm 0.4$ mrad at 240 MeV/c in LiH. These results are larger than the GEANT4 predictions, but smaller than the predictions based on the PDG scattering formula.

The momentum dependence of scattering was examined by considering 200 ps TOF selections from the muon beam data in additions to nominal momenta. This momentum dependence was compared to the dependence in Eq.10 and it was found that the RMS scattering is consistent with the PDG prediction while the widths taken from the projected scattering angles is systematically less than the prediction. Again, GEANT underestimates the scattering at all momenta, although the deviation decreases to be within uncertainties near momenta of 240 MeV/c.

The Xenon data has not been studied as well. The simulation is not as well understood for the Xenon gas as the lithium hydride. The GEANT4 simulation shows tails that do not appear in data or the Carlisle-Cobb simulation while the width of the scattering distribution is more consistent with the GEANT4 simulation both in

Table 11: The results of the fit of $a/p\beta + b$ to the scattering widths as a function of momentum. The value consistent with the PDG prediction is also shown.

Angle	a (mrad)	b (mrad)
Θ_X	237 ± 10	-0.7 ± 0.7
Θ_Y	241 ± 10	-0.8 ± 0.7
$\sqrt{\langle \theta_{Scatt}^2 \rangle} / 2$	243 ± 13	0.2 ± 0.8
PDG	250	0

terms of the χ^2 between the data and the convolution and the measured scattering width. When the convolution with the GEANT simulation is used to provide the deconvolution response, the measured scattering width in Xenon gas is $7.06 \pm 0.12 \pm 0.06$ mrad were the expected scattering was 8.76 mrad from the PDG calculation or 6.72 mrad from GEANT4.

260

References

- 265 [1] **MICE** Collaboration, D. Adams *et al.*, “Characterisation of the muon beams for the Muon Ionisation Cooling Experiment,” *Eur. Phys. J.* **C73** no. 10, (2013) 2582, `arXiv:1306.1509`
[physics.acc-ph].
- [2] D. Attwood *et al.*, “The scattering of muons in low Z materials,” *Nucl. Instrum. Meth.* **B251** (2006) 41–55, `arXiv:hep-ex/0512005` [hep-ex].
- 270 [3] **MuScat** Collaboration, W. J. Murray, “Comparison of MuScat data with GEANT4,” *Nucl. Phys. Proc. Suppl.* **149** (2005) 99–103. [,99(2005)].
- [4] **GEANT4** Collaboration, S. Agostinelli *et al.*, “GEANT4: A Simulation toolkit,” *Nucl. Instrum. Meth.* **A506** (2003) 250–303.
- [5] L. Urban, “A model for multiple scattering in Geant4,”.
- 275 [6] T. Carlisle, *Step IV of the Muon Ionization Cooling Experiment (MICE) and the multiple scattering of muons*. PhD thesis, Oxford U., 2013.
`http://mice.iit.edu/phd/TimCarlisle-thesis.pdf`.
- [7] G. D’Agostini, “A Multidimensional unfolding method based on Bayes’ theorem,” *Nucl. Instrum. Meth.* **A362** (1995) 487–498.
- 280 [8] T. Adye, “Unfolding algorithms and tests using RooUnfold,” in *Proceedings of the PHYSTAT 2011 Workshop, CERN, Geneva, Switzerland, January 2011, CERN-2011-006, pp 313-318*, pp. 313–318. 2011.
`arXiv:1105.1160` [physics.data-an].
`http://inspirehep.net/record/898599/files/arXiv:1105.1160.pdf`.